

<https://doi.org/10.1038/s41528-024-00346-8>

# Strong and high-conductivity hydrogels with all-polymer nanofibrous networks for applications as high-capacitance flexible electrodes

Check for updates

Huimin He<sup>1,2,3,9</sup>, Yaqing Chen<sup>2,4,9</sup>, Aoyang Pu<sup>5</sup>, Li Wang<sup>6</sup>, Wenxiu Li<sup>5</sup>, Xiaoyu Zhou<sup>1,5,7</sup>, Chuyang Y. Tang<sup>6</sup>, Kiwon Ban<sup>5</sup>, Mengsu Yang<sup>1,5</sup>✉ & Lizhi Xu<sup>2,4,8</sup>✉

Flexible devices, such as soft bioelectronics and stretchable supercapacitors, have their practical performance limited by electrodes which are desired to have high conductivity and capacitance, outstanding mechanical flexibility and strength, great electrochemical stability, and good biocompatibility. Here, we report a simple and efficient method to synthesize a nanostructured conductive hydrogel to meet such criteria. Specifically, templated by a hyperconnective nanofibrous network from aramid hydrogels, the conducting polymer, polypyrrole, assembles conformally onto nanofibers through in-situ polymerization, generating continuous nanostructured conductive pathways. The resulting conductive hydrogel shows superior conductivity ( $72 \text{ S cm}^{-1}$ ) and fracture strength (27.2 MPa). Supercapacitor electrodes utilizing this hydrogel exhibit high specific capacitance ( $240 \text{ F g}^{-1}$ ) and cyclic stability. Furthermore, bioelectrodes of patterned hydrogels provide favorable bioelectronic interfaces, allowing high-quality electrophysiological recording and stimulation in physiological environments. These high-performance electrodes are readily scalable to applications of energy and power systems, healthcare and medical technologies, smart textiles, and so forth.

Flexible devices have drawn surging attention due to their critical role in applications of energy harvesting and storage<sup>1,2</sup>, human-machine interactions<sup>3,4</sup>, and personalized healthcare<sup>5,6</sup> in modern society. For instance, soft bioelectronics in close contact with biological systems has been extensively explored for electrical modulation of tissues and organs, diagnosis, drug delivery, etc.<sup>7–9</sup>. Stretchable supercapacitors undergo rapid progress and are becoming a necessary unit for energy storage and supply in wearable electronic devices, due to their high power density and long-term stability<sup>10,11</sup>. To guarantee reliable functions of flexible devices in practical applications, high-performance electrodes are demanded to possess superior electrical/electrochemical, mechanical, and stability properties

simultaneously in one material system<sup>12,13</sup>. Traditional electrodes made from metals have high electrical conductivity, but their limited capacitive properties result in compromised electrode performance at low-frequency currents<sup>14</sup>. Surface modification with nanoarchitectures provides a promising way to improve the capacitive performance of electrodes. For instance, conventional electrode materials, such as carbon, platinum, and titanium nitride, elaborated with nanostructured surfaces exhibit markedly enhanced capacitance and charge injection limits<sup>15</sup>. However, nanostructuring processes may interfere with the structural integrity and bring ‘dead’ volumes, leading to the deterioration of electrode performance and the emergence of other complications<sup>11</sup>.

<sup>1</sup>Department of Precision Diagnostic and Therapeutic Technology, City University of Hong Kong Shenzhen Futian Research Institute, Shenzhen, 518057, China.

<sup>2</sup>Department of Mechanical Engineering, The University of Hong Kong, Hong Kong, China. <sup>3</sup>Institute for Frontier Science, Nanjing University of Aeronautics and Astronautics, Nanjing, China. <sup>4</sup>Advanced Biomedical Instrumentation Centre Limited, Hong Kong, China. <sup>5</sup>Department of Biomedical Sciences, and Tung Bio-medical Sciences Centre, City University of Hong Kong, Hong Kong, China. <sup>6</sup>Department of Civil Engineering, The University of Hong Kong, Hong Kong, China.

<sup>7</sup>Key Laboratory of Biochip Technology, Biotech and Health Centre, Shenzhen Research Institute of City University of Hong Kong, Shenzhen, China. <sup>8</sup>Materials Innovation Institute for Life Sciences and Energy (MILES), The University of Hong Kong Shenzhen Institute of Research and Innovation (HKU-SIRI), Shenzhen, 518057, China. <sup>9</sup>These authors contributed equally: Huimin He, Yaqing Chen. ✉e-mail: [bhmyang@cityu.edu.hk](mailto:bhmyang@cityu.edu.hk); [xulizhi@hku.hk](mailto:xulizhi@hku.hk)

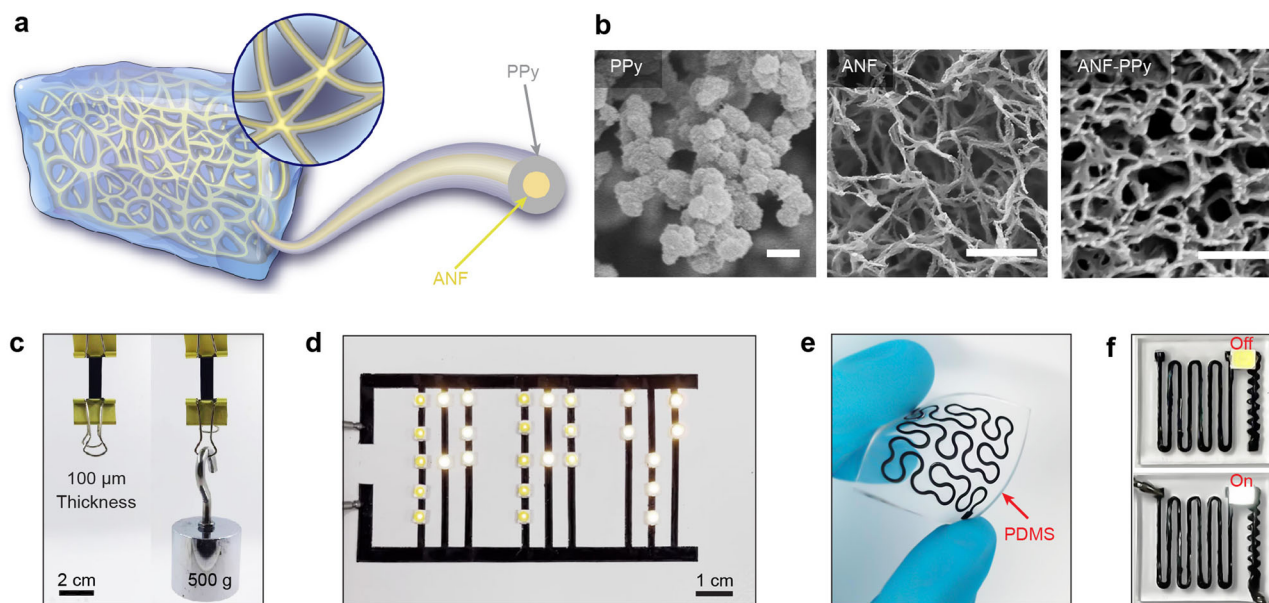


**Fig. 1 | Fabrication of ANF-PPy.** **a** A schematic illustrating the architecture of ANF-PPy. **b** SEM images showing the nanostructures of PPy polymerized in water without templates (left), ANF nanofibrous network (middle), and ANF-PPy with PPy polymerized within the ANF hydrogel network (right). Scale bar: 500 nm. **c** A thin ANF-PPy film of 100  $\mu\text{m}$  thickness loaded with 500 g

weight, demonstrating its good mechanical strength. **d** An electrical circuit with LEDs interconnected by laser-patterned ANF-PPy leads. **e** An ANF-PPy of Peano curve printed on a soft PDMS. **f** A soft electronic circuit built with a serpentine ANF-PPy to link an LED light on a soft PDMS (2 cm  $\times$  2 cm).

Electrically conductive hydrogels are highly hydrated materials with inherent porosity, simultaneously allowing efficient mass and charge transfer within the materials. Recently, electrodes comprising conducting-polymer-based hydrogels (i.e., nonconductive hydrogel matrices incorporated with conducting polymers) have been extensively explored for device applications due to their favorable electrochemical and mechanical properties, stability, and biocompatibility<sup>16–18</sup>. However, conducting polymer hydrogels produced by simply mixing or polymerizing conducting polymers within hydrogel matrices typically show compromised electrical conductivity below  $0.2 \text{ S cm}^{-1}$ , as well as high electrical percolation threshold, due to arbitrary conductive pathways built by conducting polymers<sup>14</sup>. Notably, nanostructuring conducting polymer into nanoscale networks allows the achievement of conductive hydrogels with excellent electrical conductivity (e.g.,  $\sim 10 \text{ S cm}^{-1}$ ), as exemplified by the bi-continuous nanonetworks of poly(3,4-ethylenedioxythiophene):polystyrene sulfonate (PEDOT:PSS) and hydrophilic polyurethane prepared by phase separation<sup>9</sup>. Although PEDOT:PSS-based conductive hydrogels have achieved significant success on their electrical conductivity, such structural merits and properties are still difficult to be replicated to other material systems.

Here, we develop a novel materials system to achieve strong and high-conductivity hydrogels as high-performance flexible electrodes for various device applications. Distinct from the aforementioned approaches, a nanostructured conductive network is built via conformal assembly of a conducting polymer (polypyrrole (PPy)) onto a well-established nanofibrous network originating from aramid nanofibers (ANFs) (Fig. 1a). The resulting ANF-PPy hydrogels (ANF-PPy) with hybrid hyperconnective networks present a series of superior properties distinguishable from those of other conductive hydrogels: (i) Topological conducting pathways depending on hyperconnective nanofibrous networks from aramid hydrogels enable hydrogels with superior conductivity; (ii) The nanostructured conducting polymers in-situ polymerized on nanofibers allow hydrogels with outstanding specific capacitance; (iii) Hydrogels with strengthened nanofibrous networks by bridging neighbor nanofibers with PPY show extremely high strength; (iv) Simple fabrication process of the hydrogels facilitates the facile patterning of the conductive hydrogels for high-performance electrodes. The novel strategy to fabricate ANF-PPy

nanofibrous conductive hydrogel creates new opportunities for electrode design which can be readily scalable to a wide range of flexible devices.

## Results

### Fabrication and structures

ANF-PPy conductive hydrogel (ANF-PPy) is fabricated by in-situ polymerization of PPy within an ANF hydrogel network. To enhance the conductivity of ANF-PPy, a high solid content of ANF hydrogels is preferred for serving as a dense nanofibrous template for the following PPy growth (Supplementary Fig. 1). Thus, ANF hydrogel (7 wt% solid content) is prepared by solvent exchange of high-concentration ANF dispersion (5 wt%) with pure water. Pyrrole monomers permeate the nanofibrous network of ANF hydrogels and then undergo chemical oxidative polymerization initiated by ferric chloride ( $\text{FeCl}_3$ ) as an oxidant. Notably, a highly connective network of PPy is generated based on ANF templates (Fig. 1b). In contrast, nanoparticle morphology is observed in PPy polymerized in water solution in the absence of an ANF template. ANF-PPy conductive hydrogel has an all-polymer nanofibrous network which leads to its superior mechanical and electrical properties. High strength and flexibility of the hydrogel are illustrated by a slice of ANF-PPy (7 mm width; 0.1 mm thickness) holding a weight of 500 g (Fig. 1c) or bearing substantial bending and twisting without structural damage (Supplementary Fig. 2). Furthermore, due to the facile fabrication process of ANF-PPy, various patterning techniques can be used to generate arrays of interconnects or electrodes. For instance, laser cutting of an ANF-PPy film enables interconnects to power an array of light-emitting diodes (LEDs) (Fig. 1d). Additionally, ANF-PPy conductive patterns can be fabricated on soft PDMS via microfluidic channels (details to be presented in Fig. 6), demonstrating its potential applications for flexible electronics (Fig. 1e, f).

Structural information of ANF-PPy was revealed by both molecular dynamics (MD) simulations and Fourier transform infrared spectroscopy (FTIR). For further understanding of the underlying assembling mechanism, MD simulations were first conducted to research the ternary system of pyrrole,  $\text{H}_2\text{O}$ , and ANFs (Fig. 2a, b). The binding free energy between pyrrole and ANF surpasses those between other molecules, resulting in a localized high-concentration area of pyrrole near ANF surface. An accelerated polymerization process occurs in this localized area, initiating PPy

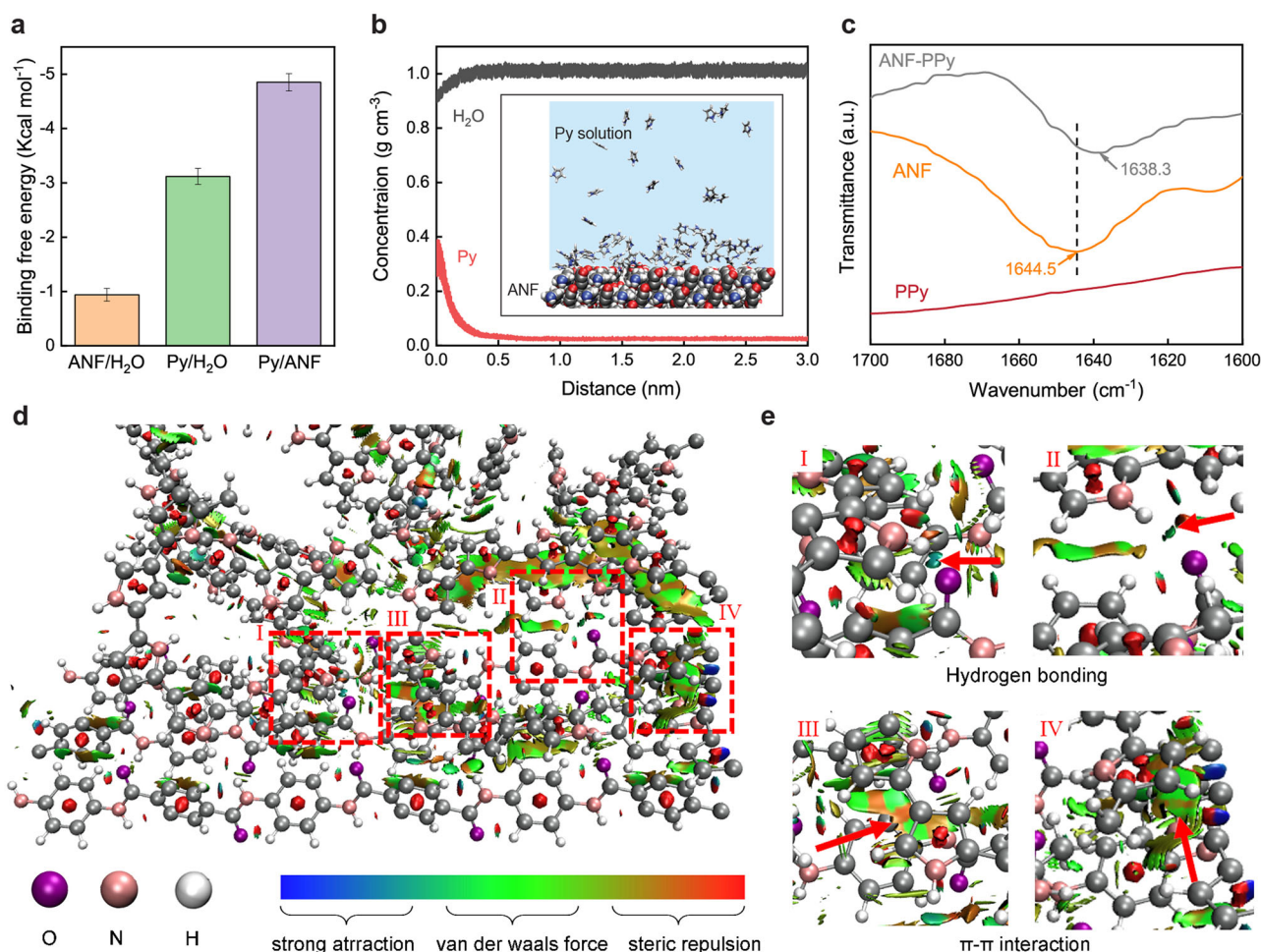


**Fig. 2 | Intermolecular noncovalent interactions.** **a** Binding free energy between ANF, H<sub>2</sub>O, and Py molecules. **b** Distribution of H<sub>2</sub>O and Py molecules in localized area near ANF surface. **c** FTIR plots showing spectra of aramid C=O stretching vibration. **d** Reduced density gradient (RDG) function isosurface map of ANF and

PPy. **e** Magnified display of the corresponding area in RDG function isosurface map, showing the existence of hydrogen bonding and  $\pi$ - $\pi$  interaction between ANF and PPy.

deposition on ANFs from the perspective of chemical kinetics. The constituents of the resulting composite hydrogel were validated by FTIR, indicating the successful polymerization process (Supplementary Fig. 3). Magnified plots shows that ANF-PPy has a slight red shift of C=O stretching vibration compared with ANF, indicating the effects of hydrogen bonding between ANF and PPy (Fig. 2c)<sup>14</sup>. Additionally, MD simulations with noncovalent interaction method according to the reduced density gradient function<sup>19</sup> were performed to research the noncovalent intermolecular interactions of ANF-PPy composite (Fig. 2d, e). Extensive noncovalent interactions of hydrogen bonding and  $\pi$ - $\pi$  interactions exist between PPy and ANFs, which also supports the conformal assembling of PPy from the perspective of thermodynamics.

### Electrical and electrochemical properties

We first researched the effect of PPy content on the conductivity of ANF-PPy (Fig. 3a). As PPy is the only conductive component, it can be conceived that low PPy content ( $\leq 1.4$  wt%) results in composite hydrogel without electron-transport abilities. However, there is a sharp increase in the conductivity when PPy content reaches a specific threshold, indicating PPy percolates in the 3D network. Notably, the percolation threshold for PPy in the composite is exceptionally low at  $\sim 2$  wt%, much lower than the value ( $\sim 20$  vol%) for randomly distributed nanoparticles<sup>20,21</sup>. This feature benefits from the unique conductive pathways guided by ANF nanofibrous templates, allowing engineering conductive composite with a minimal dosage of electroactive fillers. With a further increase in the PPy

content to  $\sim 42.1\%$  by using a high concentration of Py solution (0.6 M), the conductivity of ANF-PPy ( $\sim 46.3\%$  solid content; 100  $\mu\text{m}$  thickness) reaches an exceptionally high value of  $\sim 72 \text{ S cm}^{-1}$ , outperforming those of other PPy-based conductive hydrogels by several orders of magnitude<sup>16,18</sup>. Scanning electron microscopy (SEM) images in Fig. 1b present initial evidence on the conformal assembly of PPy on ANFs, as ANF-PPy shows markedly thicker nanofibers than ANF. The conformal coating of PPy forms a shell around the ANF cores with a thickness able to reach tens of nanometers<sup>22</sup>. This structural information can also be revealed by its distinguished electrical attributes of the ultralow PPy percolation threshold and their superhigh conductivity.

The nanostructures of conductive fillers in composite materials can have decisive effects on their electrical performance. For instance, conductive composites involving Ag nanowires show lower percolation threshold and higher conductivity than those involving Ag nanoparticles at a same doping level<sup>23</sup>. For this case, we attribute the distinguished electrical attributes of ANF-PPy to two main reasons. First, its unique assembly onto ANFs allows the formation of favorable nanofibrous architecture, which is beneficial for the building of conductive pathways within the hydrogel matrix. Second, ANF hydrogel generated by solvent exchange has a self-assembled nanofibrous network with distinctively high nodal connectivity at fiber-fiber junctions, which facilitates electron transport between fibers after conformal coating of PPy onto the nanofibrous network. As a result, ANF-PPy has a superior conductivity than other conductive hydrogels based on PPy (Supplementary Fig. 4).

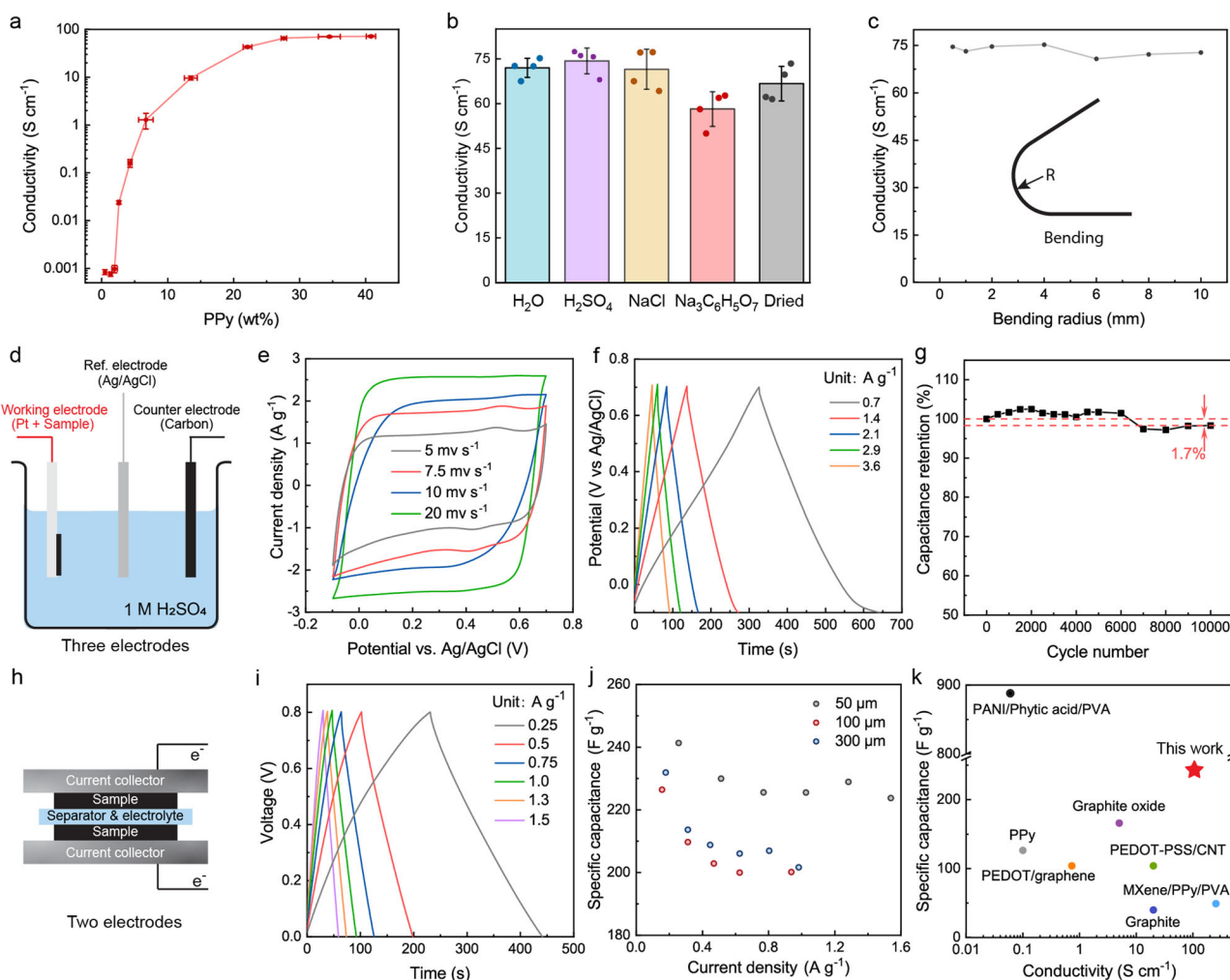


**Fig. 3 | Electrochemical properties of ANF-PPy.** **a** A correlation between the conductivity and PPy content for ANF-PPy. **b** The conductivity of ANF-PPy in various chemical environments. **c** The conductivity of ANF-PPy under various bending radius, showing good stability. **d** A schematic of three-electrode configuration for capacitance characterization. **e, f** Capacitance of ANF-PPy determined by cyclic voltammetry (CV) (**e**) and galvanostatic charge/discharge (GCD) (**f**) curves with different scan rates. **g** Capacitance retention during 10,000 charging/

discharging cycles. **h** A schematic of two-electrode configuration for capacitance characterization. **i** Capacitance of ANF-PPy characterized by GCD at different current density. **j** Gravimetric capacitance at different current density for ANF-PPy with varying thickness. **k** Comparison of conductivity and gravimetric capacitance between ANF-PPy and other reported supercapacitor electrodes. Data points were categorized based on Table S1, Supporting Information. Data in **a** and **b** are reported as their means  $\pm$  SDs from  $n = 4$  independent samples.

The electrical stability of ANF-PPy under various chemical environments and large-scale mechanical deformation is critical for its device applications. For instance, supercapacitor electrodes generally work in acidic or salt-rich solutions<sup>24</sup>, while electrodes for soft bioelectronics need to tolerate substantial mechanical deformation in wearable or implantable applications<sup>25</sup>. The chemical inertness of ANF-PPy was characterized by soaking ANF-PPy in H<sub>2</sub>SO<sub>4</sub> or saline solution of NaCl and sodium citrate at a high concentration of 1 M respectively (Fig. 3b). ANF-PPy treated with H<sub>2</sub>SO<sub>4</sub> and NaCl solution has a minimal change on the conductivity. ANF-PPy in the sodium citrate solution experiences a slight decrease in conductivity but still keeps a high value at  $\sim 58$  S cm<sup>-1</sup>, possibly due to the reducibility of sodium citrate which may interfere with the doping state of PPy<sup>26</sup>. Furthermore, the conductivity of ANF-PPy after the removal of the solvent by critical point drying is  $\sim 67$  S cm<sup>-1</sup>, indicating its applicability at dry conditions. On the other hand, the electrical stability of ANF-PPy under deformation was determined by its conductivity as a function of the bending radius. ANF-PPy shows negligible changes in the conductivity even at an extreme condition with a bending radius of 0.5 mm (Fig. 3c), indicating its superior flexibility for soft-device applications. The long-term stability of the conductivity of ANF-PPy was confirmed by its consistent high level of conductivity during soaking in water for 7 days (Supplementary Fig. 5).

We research the performance of ANF-PPy as supercapacitor electrodes in both three-electrode and two-electrode configurations. For a three-electrode configuration, ANF-PPy on a Pt electrode is used as the working electrode, with a counter electrode of carbon and a reference electrode of Ag/AgCl (Fig. 3d). Initial information about the capacitance of ANF-PPy electrode is provided by cyclic voltammetry (CV) curves (Fig. 3e). The CV curves have a quasi-rectangular shape with almost constant current during charging at varying scan rates, exhibiting an ideal behavior of electrochemical double layers<sup>10</sup>. At low scan rate of 5 and 7.5 mV s<sup>-1</sup>, the gravimetric capacitances are 213.8 and 199.3 F g<sup>-1</sup> respectively. ANF-PPy shows a typical scan rate dependence with gravimetric capacitances of 151.3 and 106.6 F g<sup>-1</sup> at scan rates of 10 and 20 mV s<sup>-1</sup> respectively, partially due to the incomplete developing of capacitance at high scan rates<sup>27</sup>. We used the Trasatti method to reveal the scan rate-dependent capacitance of ANF-PPy by plotting the reciprocal of specific capacitance against the square root of scan rate (Supplementary Fig. 6). Presumably, when the scan rate approaches 0 mV s<sup>-1</sup>, ions have enough time to diffuse to the entire hydrogel electrode for charge storage. In this case, the ANF-PPy capacitance reaches its highest value, where the capacitance is irrelevant to the ion diffusion rate. In the slow scan rate region, the plot was fitted with a straight line and extrapolated to the y-axis. The ideal capacitance is equal to the reciprocal of

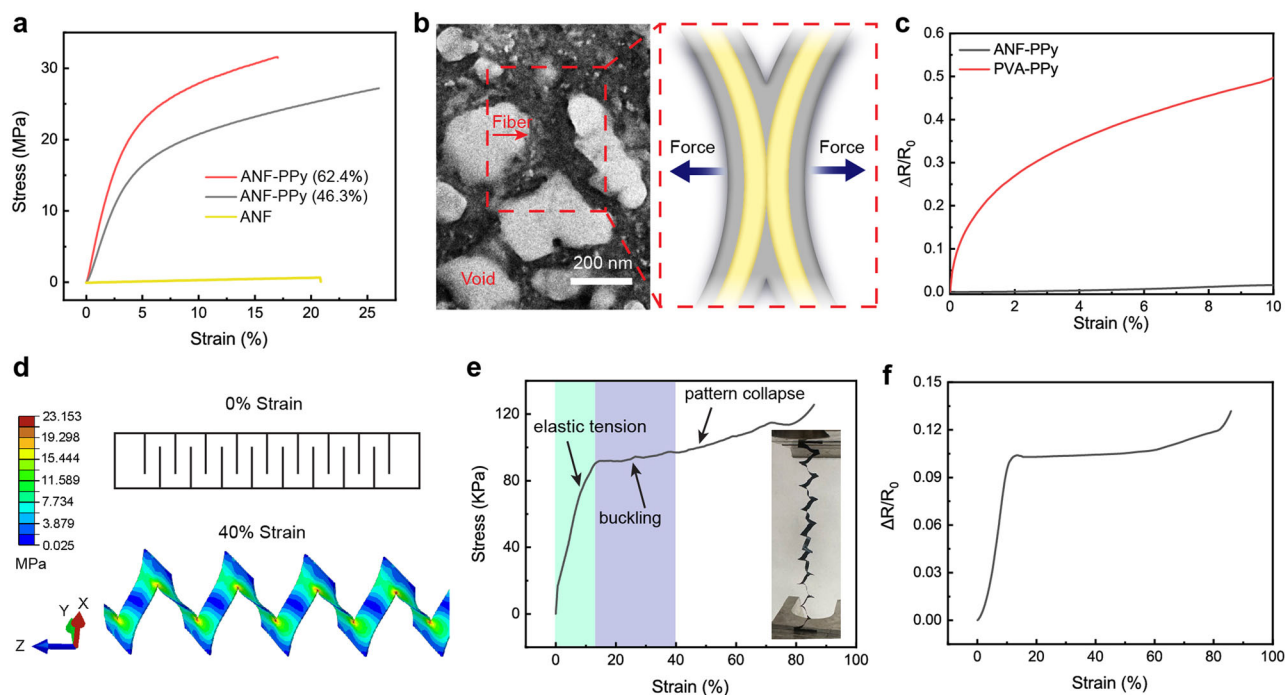


**Fig. 4 | Mechanical and electrical behaviors under deformation.** **a** Stress-strain curves for ANF hydrogels with or without PPy composition. **b** Morphology of ANF-PPy network visualized by TEM (left) and a schematic illustrating PPy-reinforced bonding between neighbor ANFs. **c** Resistance change under tension for ANF-PPy and PVA-PPy hydrogels. **d** A schematic of a kirigami ANF-PPy (1 cm × 5 cm) with

17 periodic laser-cut slits. The FEM snapshot shows the stress distribution of the kirigami ANF-PPy at 40% tensile strain. **e** A typical stress-strain curve for the kirigami ANF-PPy, involving an initial elastic region (green), buckling region (purple), and pattern-collapse region (white). **f** Resistance change under tension for the Kirigami ANF-PPy.

the y-intercept, as calculated to be  $316 \text{ F g}^{-1}$ . More definite information of the capacitance is carried by galvanostatic charge/discharge (GCD) curves (Fig. 3f). Tailing of curves at the end of discharge was observed under low discharge rate, which may be attributed to the proton-associated reactions in acidic conditions at low potentials with the presence of Pt and electroactive polymers<sup>28,29</sup>. To eliminate the effect of tailing parts on the capacitance measurements, the slope of the discharge curve over the range of the first-half part was used to calculate hydrogel capacitance (details to be presented in the “Methods” section). The gravimetric capacitance kept consistent between 200.3 and  $202.3 \text{ F g}^{-1}$  at varying current density from 0.7 to  $3.6 \text{ A g}^{-1}$ . Both methods demonstrate ANF-PPy electrode has an excellent capacitance over  $200 \text{ F g}^{-1}$ . Furthermore, the capacitance of ANF-PPy only has 1.7% drop after 10,000 charging/discharging cycles at a high scan rate of  $80 \text{ mV s}^{-1}$ , demonstrating remarkable stability in comparison with other supercapacitors<sup>13,30</sup> (Fig. 3g).

As the best-practice method for determining the capacitance of electrodes, a two-electrode symmetrical supercapacitor cell based on two ANF-PPy plates separated by a glass paper permeated with  $\text{H}_2\text{SO}_4$  electrolyte (1 M) is used to determine the capacitance according to GCD cycles (Fig. 3h and i). The specific capacitances normalized with area, volume, and weight are all measured for ANF-PPy electrodes with different thickness of about 50, 100, and  $300 \mu\text{m}$  respectively (Fig. 3j and Supplementary Fig. 7). The areal capacitance increases with the thickness of electrodes because more electroactive material of PPy is involved in thicker electrodes. As a vital parameter signifying the performance of a supercapacitor, the areal capacitance of ANF-PPy reaches  $1040.5 \text{ mF cm}^{-2}$  at a thickness of  $300 \mu\text{m}$ , outperforming most of recent supercapacitor electrodes (Supplementary Table 1). In contrast, the volumetric capacitance decreases with the thickness of electrodes, which is caused by the inhomogeneous distribution of PPy within the hydrogel network (i.e., the PPy contents of ANF-PPy decreases with the thickness) (Supplementary Table 2). Nevertheless, the gravimetric capacitance has a narrow distribution between 200 and  $240 \text{ F g}^{-1}$  with different electrode thickness, indicating stable conductive pathways built by the efficient assembly of PPy. Furthermore, the

comparable capacitance values measured under three-electrode and two-electrode configurations provide support for the robustness of the test methods. Overall, ANF-PPy electrodes show superior properties on both conductivity and capacitance, compared with other supercapacitor electrodes (Fig. 3k and Supplementary Table 1). Specifically, the conductivity of ANF-PPy exceeds those of other PPy-based hydrogels by several orders of magnitude, arising from its unique hyperconnective nanofiber networks. Additionally, its gravimetric capacitance is also much higher than those of other ppy-based electrodes and even surpasses those of graphite-based electrodes which have significantly lower density. We attribute these properties to its extensive open networks and electrically active interfaces.

### Mechanical performance

Incorporation of PPy into ANF networks leads to a marked enhancement on the mechanical strength (Fig. 4a). Pure ANF hydrogel (7% solid content;  $100 \mu\text{m}$  thickness) has a tensile strength of  $\sim 0.9 \text{ MPa}$  and a Young’s modulus of  $\sim 4.8 \text{ MPa}$ . Compared with the intrinsic strength and Young’s modulus of para-aramid fibers<sup>31</sup>, the mechanical properties of ANF hydrogels are compromised, which may arise from the weak interactions between nanofibers and their disintegration under imposed deformation<sup>32</sup>. Notably, the incorporated PPy bridges the neighbor nanofibers to facilitate load transfer within the network, as visualized by TEM images of ANF-PPy (Fig. 4b). The establishment and reinforcement of binding nodes between nanofibers have been proved to significantly enhance the mechanical performance of nanofibrous network<sup>33,34</sup>. As a result, the ANF-PPy hydrogel ( $\sim 46.3\%$  solid content;  $100 \mu\text{m}$  thickness) with incorporated PPy at  $\sim 42.1 \text{ wt } \%$  content shows a superior strength and Young’s modulus at  $\sim 27.2$  and  $\sim 512.3 \text{ MPa}$  respectively, along with a ductility at  $\sim 22.4\%$ . The toughness of ANF-PPy was quantified by fracture energy of about  $5.3 \times 10^8 \text{ J m}^{-3}$ , calculated from the integration of the stress-strain curve<sup>35</sup>. Lowering the thickness of ANF film facilitates mass diffusion within the hydrogel network during the PPy polymerization process, leading to an ANF-PPy composite ( $\sim 62.4\%$  solid content;  $50 \mu\text{m}$  thickness) with high PPy content at  $\sim 59.3\%$ . This ANF-PPy composite has a high conductivity of  $\sim 106 \text{ S cm}^{-1}$  and

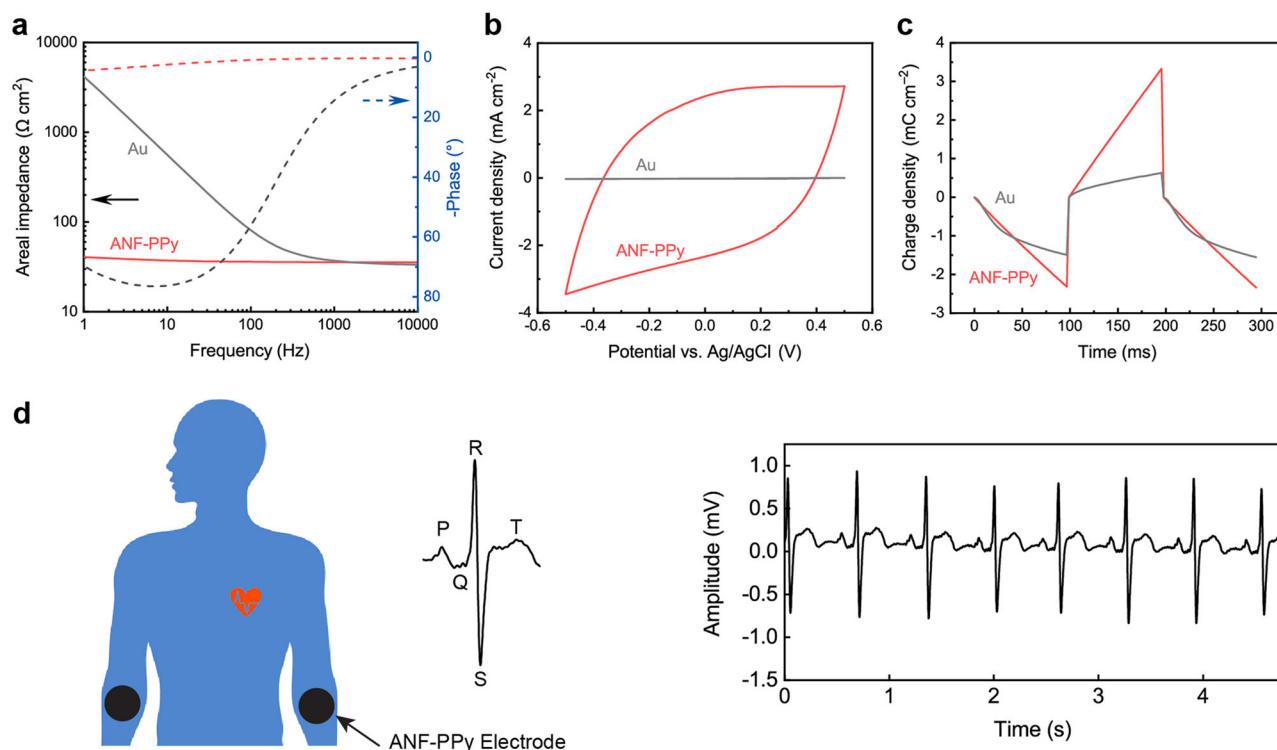


**Fig. 5 | Bioelectrodes based on ANF-PPy.** **a** Electrochemical impedance spectroscopy (EIS) measurements for ANF-PPy and an Au foil. **b** CV curves for ANF-PPy and an Au foil. **c** Cyclic electrochemical current pulse injection curves of electrodes based on ANF-PPy and an Au foil with a square wave between  $-0.5 \text{ V}$  and  $0.5 \text{ V}$ .

**d** High-quality ECG signals were recorded by ANF-PPy electrodes with clear QRS, P, and T waves. All electrodes have the same thickness of  $100 \mu\text{m}$  and were tested in PBS using an Ag/AgCl electrode as a reference.

excellent strength and Young's modulus at  $\sim 31.8$  and  $\sim 716.3 \text{ MPa}$  respectively (Supplementary Table 2).

Stability of electrical resistance under applied deformation is a favorable attribute for conductive materials in many scenarios of device applications<sup>36</sup>. ANF-PPy ( $\sim 46.3\%$  solid content;  $100 \mu\text{m}$  thickness) with a high conductivity of  $72 \text{ S cm}^{-1}$  only has a negligible resistance change upon 10% tensile strain, showing a gauge factor calculated to be as low as 0.16 (Fig. 4c). The strain-invariant electrical properties of ANF-PPy originates from nanofiber alignment during the deformation, which preserves the intrinsic topology of the conductive pathways<sup>14</sup>. For comparison, a control sample is employed with PPY polymerized within a PVA hydrogel. In this case, PPY nanoparticles are randomly distributed within the PVA hydrogel matrix, leading to a low conductivity of  $0.08 \text{ S cm}^{-1}$ . The resistance of PVA-PPy hydrogel increased by  $\sim 50\%$  under 10% tensile strain, due to the increase of distance between PPY particles and increased barrier for electron tunneling<sup>21,37</sup>.

Application of rigid materials for wearable electronics can be optimized by the reduction of material thickness and the introduction of kirigami structures<sup>38</sup>. The stretchability of ANF-PPy can be enhanced by introducing periodic laser-cut slits ( $0.75 \text{ cm}$ ) into a pristine sample ( $1 \text{ cm} \times 5 \text{ cm}$ ) (Fig. 4d). Finite element modeling (FEM) reveals that under an elongation of 40%, the peak stress in the kirigami ANF-PPy is about 23 MPa, which is below the strength of ANF-PPy. Experimental tensile tests also demonstrate the structural robustness of kirigami ANF-PPy (7% solid content;  $100 \mu\text{m}$  thickness) (Fig. 4e). The corresponding stress-strain curve shows 3 main regions: (I) The initial elastic region (green) associated with planar deformation with the strain below 13%. (II) The out-of-plane buckling region (purple) with the applied stress exceeds a critical value. The stress reaches a plateau in the buckling process (13–40% strain). (III) The final pattern-collapse region where cracks propagate due to overhigh stress at crack tips. Overall, the Kirigami ANF-PPy shows a markedly reduced Young's

modulus at a kPa level and can sustain tensile deformation above 80% before failure, which expands its applications in soft electronics<sup>39</sup>. Furthermore, the resistance change of kirigami ANF-PPy remains at a low level ( $<12\%$ ) during tension before breakage (Fig. 4f). Increase in the resistance is observed at the beginning and end of tension, resulting from the crack opening<sup>40</sup> and propagation, respectively. Kirigami ANF-PPy can withstand over 100 cycles of 20% elongation without causing significant change to the electrical resistance (Supplementary Fig. 8).

#### Patterning of electrodes for bioelectronic applications

The outstanding conductivity of ANF-PPy compared with other PPy-based hydrogels allows it to be applied in bioelectronics. The favorable bioelectronic performance of ANF-PPy is initially evidenced by its low impedance in phosphate-buffered saline (PBS) (Fig. 5a). Compared with an Au foil of the same thickness, ANF-PPy (7% solid content;  $100 \mu\text{m}$  thickness) has markedly lower areal impedance under frequency below 1000 Hz, which covers the frequency band for common bio-signals<sup>41</sup>. Alternatively, the advantages of ANF-PPy bioelectrodes are also revealed by its capability in delivering electrical stimulation. The bulk nanostructures of ANF-PPy provide high interfacial capacitance, allowing good control over the current flow with high charge storage capability and charge injection capacity (Fig. 5b, c). The low impedance allows ANF-PPy to be used as a bioelectrode to record physiological signals, such as electrocardiograph (ECG) signals, with high quality (Fig. 5d). The capacitive nature of ANF-PPy electrodes can avoid non-reversible Faradaic reactions which may bring electrode degradation and harmful byproducts during electrical stimulation<sup>42</sup>.

To pattern ANF-PPy for custom-built bioelectrodes, we prepared a PDMS mold containing microchannels by microfabrication techniques. The PDMS mold was covered with a water-soluble tape, and ANF dispersion (3 wt%) was infused from the inlet into the microchannel (Fig. 6a). Patterned ANF hydrogel is generated by soaking the PDMS in water for the

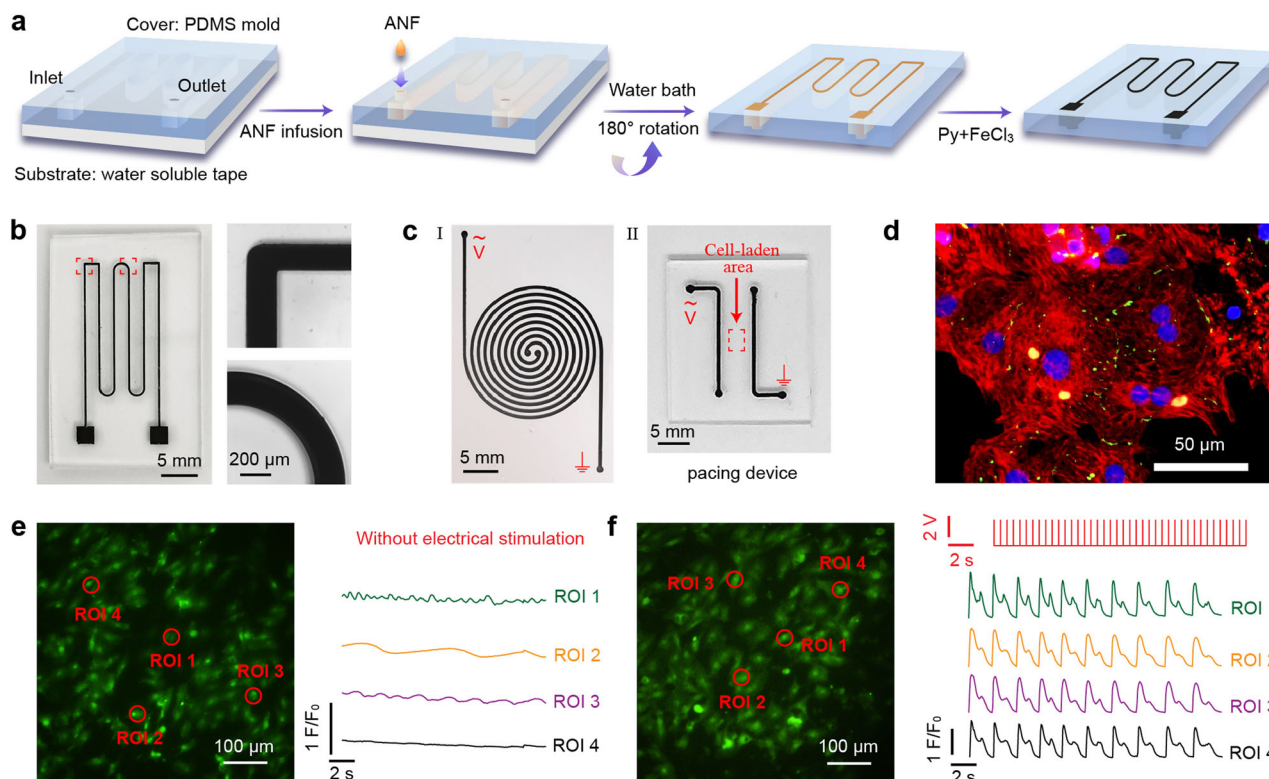


**Fig. 6 | Patterned bioelectrodes for electrical stimulation.** **a** Schematics of the printing process for patterned ANF-PPy on a soft PDMS substrate. **b** Optical images of a representative ANF-PPy pattern with right-angle and curve corners. **c** Capacitive bioelectrodes based on two parallel ANF-PPy electrodes of spiral or liner assembly respectively. **d** Immunofluorescent staining of cardiomyocytes

cultured on ANF-PPy for 5 days. Cardiac-specific proteins of troponin T (red) and connexin-43 (green), and nucleus (blue) were fluorescently labeled. **e, f** Imaging of calcium transients for cardiomyocytes cultured on ANF-PPy-PDMS without (**e**) or with (**f**) electrical stimulation. Traces of fluorescence intensity at different regions of interest (ROI) were recorded to show the pacing state of cardiomyocytes.

removal of the tape and solidification of ANF dispersion. After that, a final ANF-PPy pattern embedded within the PDMS channel is achieved through the incorporation of PPy into the hydrogel network by sequential treatment with Py and  $\text{FeCl}_3$  solutions. The successful printing of ANF-PPy on PDMS is demonstrated by high-resolution features of 200- $\mu\text{m}$ -wide lines or right-angle and curved turns (Fig. 6b).

To demonstrate the capability of ANF-PPy bioelectrodes for electrical stimulation, we printed two parallel ANF-PPy electrodes on PDMS (Fig. 6c). First, cardiomyocytes (CMs) seeded on the surface of ANF and ANF-PPy hydrogels shows great cell viability, in which ANF-PPy exhibits slightly better CM attachment as compared with the bare ANF substrate (Supplementary Fig. 9). This result may originate from the protein-affinity of ANF-PPy with appropriate hydrophilicity<sup>43</sup> (Supplementary Fig. 10). The lack of hydrophilic components of ANF-PPy incurs the easy loss of water from hydrogel (Supplementary Fig. 11), indicating its applications applicable in moisture environments. The favorable interface between the ANF-PPy electrodes and cells is further validated by fast maturation of CMs cultured on ANF-PPy, as evidenced by pronounced expression of typical cardiac markers of troponin T and connexin-43 for CMs after culture of 5 days (Fig. 6d and Supplementary Fig. 12). The great biocompatibility of ANF-PPy hydrogels were further revealed by cells with high viability and fast proliferation cultured on hydrogels (Supplementary Fig. 13). A pacing device was constructed with CMs laden in the area between two electrodes<sup>44,45</sup>. Two linear ANF-PPy electrodes (0.3 mm thickness, 0.6 mm width, and 20 mm length) were printed on PDMS with the gap width between two parallel electrodes of 5 mm (Fig. 6c (II)). Due to the capacitive nature of electrodes, bioelectrical stimulations can be delivered through charging and discharging the electrodes without non-reversible Faradaic reactions. Previous research has revealed that long-time electrical stimulation by pulsatile electrical fields can accelerate the maturation of CMs and generate synchronously contractile cardiac

constructs<sup>42</sup>. In our experiment, we first cultured CMs on the device for 3 days without electrical stimulation, which led to weak and random excitation CMs as evidenced through calcium imaging (Fig. 6e). However, after application of monophasic electrical pulses (2 Hz) for 10 min through the ANF-PPy electrodes, overdrive pacing of these immature CMs was achieved. The contraction rate synchronized to the frequency of 1 Hz, half the value of the pacing frequency (Fig. 6f and Supplementary Video 1). After each synchronized calcium spike, immature CMs take a long period of about 2 s to reduce the calcium concentration to the baseline level. Between two calcium spikes, a much weaker excitation is observed at high intracellular calcium concentrations, which is compulsorily driven by external electrical stimulation. This compulsory excitation at high intracellular calcium concentrations may enhance CMs' capability in calcium ion transport and facilitate their synchronized contraction at higher frequencies after a long-time electrical stimulation<sup>42</sup>.

## Discussion

In summary, we developed a conductive nanocomposite hydrogel tailored for applications as high-performance electrochemical electrodes. The hybrid nanofiber network provides a good combination of mechanical strength, electronic conductivity, and porosity, which is beneficial for the use in flexible electronics operating under extreme physicochemical conditions. Supercapacitors involving this ANF-PPy hydrogel exhibit outstanding capacitance, which can be further utilized in miniaturized energy systems. On the other hand, the simple fabrication processes of ANF-PPy afford the patterning of stretchable bioelectrodes arrays, which exhibit excellent functionality and compatibility with living cells and tissues. Further integration of this materials platform and manufacturing techniques with other soft electronic components will enable multifunctional systems for wearable biochemical sensing, smart implants, electroactive tissue engineering constructs, and many other applications.

## Methods

### Materials and method

ANF dispersion was prepared by dissolving Kevlar para-aramid pulp (Type 979; DuPont) in a mixed solvent of DMSO and H<sub>2</sub>O (a weight ratio of 4:1 between DMSO and H<sub>2</sub>O) containing 2 wt% KOH under magnetic stirring at 90 °C for 3 days. The resulting ANF liquid dispersion was cast on a flat steel plate by a film coater, followed by solvent exchange in deionized (DI) water for 24 h to generate ANF hydrogel films. Without specific statement, ANF hydrogel (7 wt% solid content) is prepared from 5 wt% ANF dispersion in this research. For ANF-PPy synthesis, ANF hydrogel was soaked in a pyrrole solution (0.6 M, Sigma-Aldrich) under ice-water bath with vibration at a speed of 160 rpm using a shaker for 1 h. After that, FeCl<sub>3</sub> (Sigma-Aldrich) was added into the solution to achieve a concentration 1.2 times as much as the molar concentration of Py monomers for 2 h polymerization. As a contrast, PVA hydrogel was prepared by freezing PVA solution (15% in DI water; Mw: 146,000 – 186,000; 99%+ hydrolyzed; Sigma-Aldrich) at –20 °C overnight and thawing at room temperature. PVA-PPy hydrogel was achieved using the same procedures for the fabrication of ANF-PPy.

### Electron microscopy

For scanning electron microscope (SEM) imaging, the cross-sections of hydrogel were generated by cutting a hydrogel plunge-frozen in liquid nitrogen. Samples were dried by critical point drying (CPD; Tousimis Autosamdri 931) before imaging using a SEM (Hitachi S4800 FEG) with a 5 keV operating voltage. For transmission electron microscope (TEM) imaging, the ultrathin cross-sections of ANF-PPy were achieved by slicing resin-embedded dried ANF-PPy with ultramicrotomy (Leica EM UC7). The cross-sectional morphology of ANF-PPy was observed using a TEM (Philips CM100) with a 100 keV accelerating voltage.

### Theoretical simulations

Molecular dynamics (MD) simulations were conducted with GROMACS 2022 under the General AMBER Force Field (GAFF2) force field<sup>46,47</sup>. Initially, the structures of H<sub>2</sub>O, Py, and ANF molecules were constructed and optimized by Gaussian 16, and then the advanced restrained electrostatic potential charges (RESP2) of these molecules were assessed by Multiwfn 3.7 for the following simulations<sup>48,49</sup>. According to the experimental conditions, a cuboid periodic boundary condition box<sup>50</sup> (5 × 5 × 8 nm<sup>3</sup>) with a H<sub>2</sub>O-to-Py molar ratio of 90:1 was generated by random distribution. Three stacked infinite layers of ANF molecules were orderly organized through intermolecular hydrogen bonding, which was placed on the bottom of the box to act as the ANF surface. This system was further optimized by energy minimizations using 5000 steepest descent steps to exclude unfavorable organizations. After that, an equilibrium state of the system was achieved in an isothermal-isobaric ensemble at 298 K and 1 atm. Finally, a 50 ns production run was conducted, and data of the last 10 ns were collected for further analysis. The real-space cut-off for noncovalent interactions is 12 Å and the time step is 1 fs<sup>51</sup>. Long-range electrostatic interactions and van der Waals forces were calculated using the particle mesh Ewald method. Visualization process was assisted by VMD software<sup>51</sup>.

To probe the noncovalent interactions between ANF and PPy, a cuboid periodic boundary condition box (5 × 5 × 8 nm<sup>3</sup>) with a bottom layer of ANF and 45 PPy molecules<sup>48</sup> (degree of polymerization: 10) was generated. Similar to the aforementioned methods, a balanced organization between ANF and PPy was achieved after 50 ns MD simulation in an isothermal-isobaric ensemble at 298 K and 1 atm. Molecular interactions were further studied by noncovalent interaction method with Multiwfn 3.7 according to reduced density gradient (RDG) function<sup>19</sup>.

$$RDG(r) = \frac{1}{2(3\pi^2)^{1/3}} \frac{|\nabla\rho(r)|}{[\rho(r)]^{4/3}} \quad (1)$$

where  $\rho$  is electron density and  $r$  is coordinate vector. Visualization process was assisted by VMD software with the RDG isosurfaces of a cut-off value at

0.5 a.u.  $sign(\lambda_2)\rho$  mapped on the isosurfaces between –0.035 a.u. (blue) and 0.02 a.u. (red).

### Electrical conductivity measurement

Electrical conductivity was measured using a two-probe method by applying a bias voltage on both ends of a strip sample with fixed length ( $L$ , 25 mm), width ( $W$ , 4 mm), and thickness ( $T$ , 0.1 mm) using a source meter (Keithley 2450). The conductivity was calculated by

$$\kappa = \left(\frac{I}{V}\right) \left(\frac{L}{W \times T}\right) \quad (2)$$

where  $\kappa$  is the conductivity,  $V$  is the voltage, and  $I$  is the current. ANF-PPy with different PPy contents were prepared by varying pyrrole concentrations in the polymerization process. The PPy content of hydrogels was determined by weighing the ANF hydrogels before PPy loading and weighing ANF-PPy before and after drying. The ppy content was calculated by

$$C_{PPy} = \frac{W_{dry} - 7\%W_{ANF}}{W_{wet}} \times 100\% \quad (3)$$

where  $C_{PPy}$  is the weight content of PPy in ANF-PPy,  $W_{wet}$  is the weight of an ANF-PPy hydrogel,  $W_{dry}$  is the weight of the ANF-PPy after drying, and  $W_{ANF}$  is the weight of the ANF hydrogel.

For determining the conductivity of ANF-PPy in different environments, ANF-PPy strip samples were soaked in solutions of H<sub>2</sub>SO<sub>4</sub>, NaCl or sodium citrate with a fixed concentration of 1 M for 1 h. Conductivity of samples was measured immediately without any treatment after samples were retrieved from solutions. Conductivity of dried samples was measured by CPD-dried ANF-PPy.

### Characterization of supercapacitors

The performance of supercapacitors was measured by CV and GCD tests in a three-electrode configuration using an electrochemical workstation (PGSTAT302N, Metrohm Autolab). ANF-PPy mounted on a Pt grid electrode with an area of 1 × 1 cm<sup>2</sup> exposed to the electrolyte was used as a working electrode, an Ag/AgCl electrode as the reference electrode, and a graphite rod as the counter electrode in the electrolyte of H<sub>2</sub>SO<sub>4</sub> solution (1 M). Gravimetric capacitance based on CV tests was calculated by

$$C_m = \frac{S}{2m\Delta V} \quad (4)$$

where  $C_m$  is the gravimetric capacitance,  $S$  is the area enclosed by cyclic voltammetry curve,  $m$  is the mass of PPy in the working electrode,  $v$  is the scan rate, and  $dV$  is the potential window. Gravimetric capacitance based on GCD was calculated by

$$C_m = \frac{I}{m\Delta V/dt} \quad (5)$$

where  $C_m$  is the gravimetric capacitance,  $I$  is the constant discharge current,  $m$  is the mass of PPy for the working electrode, and  $dV/dt$  is determined by the slope of the discharge curve over the range of  $V_{max}$  (the voltage at the beginning of discharge) to 0.5  $V_{max}$ .

A two-electrode cell configuration was also used to determine the capacitance of ANF-PPy electrodes. Two identical (by weight and size) disk-shaped electrodes with a diameter of 10 mm were mounted in a test cell. Two current collectors of carbon cloth, one separator of a glass microfiber film (Whatman GF/A) which was permeated with H<sub>2</sub>SO<sub>4</sub> solution (1 M)



were used. Capacitance was calculated by

$$C = \frac{2I}{dV/dt} \quad (6)$$

Where  $C$  is the capacitance,  $I$  is the constant discharge current, and  $dV/dt$  is determined by the slope of the discharge curve over the range of  $V_{\max}$  to  $0.5 V_{\max}$ . Gravimetric capacitance, areal capacitance, and volumetric capacitance were calculated by dividing the capacitance with the mass of PPy, the geometric area, and volume for the working electrode respectively.

### Mechanical tests

Mechanical properties of hydrogels (fixed size of 25 mm × 4 mm × 0.1 mm) were characterized using a mechanical tester (Zwick Roell) under a tensile rate of 50% min<sup>-1</sup>. For the assessment of resistance change in response to applied strain, the resistance of samples was simultaneously recorded until fracture during the tensile tests. For compliant ANF-PPy with kirigami structures, samples were cut using infrared lasers (Ming Chuang Laser 3020). Kirigami samples with real-time resistance recording were also stretched at a tensile rate of 50% min<sup>-1</sup>.

### Finite element modeling

A model of the Kirigami sample was built and analyzed with a commercial software package (Abaqus/CAE 2021) to learn its behaviors under tension by FEM methods. A boundary condition is imposed on both ends of the mold with one end constrained to prevent any displacement. At the opposite end, an axial load is applied while the boundary is constrained from movement in orthogonal directions. The dynamic procedure was used to simulate the process between 0 and 40% strain.

### Characterization of bioelectrodes

Electrochemical impedance spectroscopy (EIS) measurements of ANF-PPy and an Au foil were conducted using a sine wave with an amplitude of 10 mV. For comparison of the capacity of charge storage and charge injection between ANF-PPy and Au electrodes, CV test was performed at a scan rate of 0.15 mV s<sup>-1</sup> between the potential window of -0.5 and 0.5 V, while square-wave voltage pulses between -0.5 and 0.5 V, each lasting 100 ms, were applied to working electrodes to collect corresponding current responses. All electrochemical tests were carried out in PBS using ANF-PPy or Au foil with an exposed area of 1 cm<sup>2</sup> as the working electrode. A Pt foil and Ag/AgCl electrode were used as the counter electrode and the reference electrode respectively for all the measurements under an electrochemical workstation.

ANF-PPy plates with a diameter of 10 mm were used as bioelectrodes to detect ECG signal by a commercial data acquisition system (PowerLab T26, AD Instruments). Three electrodes were mounted on a volunteer's left forearm, right forearm, and left leg by conductive gel. All physiological experiments were conducted following standard protocols, with explicit informed consent obtained from participating volunteers, and received approval from the Human Research Ethics Committee at The University of Hong Kong under project number EA200171.

### Cell culture

Cardiomyocytes (CMs) were harvested from the left ventricles of neonatal Sprague-Dawley rats (postnatal day 1–3). Specifically, ventricles collected from neonatal rats were cut into small pieces in ice-cold Dulbecco's Phosphate-Buffered Saline (Gibco) and then digested by trypsin (0.1%, Gibco) at 4 °C overnight. After washing with culture media (Gibco), tissues were dissociated into single cells by 3 cycles of treatment with rat collagenase type II (0.1%, Worthington) at 37 °C for 20 min. CMs were enriched by Percoll density gradient centrifugation for 30 min to remove other types of cells. The harvest of CMs from neonatal Sprague-Dawley rats was approved by the City University of Hong Kong under protocol number 11104222.

To promote CM attachment, hydrogel films were rinsed thoroughly by PBS and treated with gelatin solution (0.1%, Type B, Sigma-Aldrich) under

37 °C for 1 h. CMs (~2 × 10<sup>5</sup> cells in 25 μL media) were seeded onto samples and incubated for 1 h before adding CM-specific media (10% fetal bovine serum, 1% penicillin-streptomycin, and 1% non-essential amino acids).

CMs after 5 days of culture were stained by live-dead assay and immunocytochemistry. For live-dead staining, cells were incubated in PBS solutions of calcein-AM (green, 2 μM) and ethidium homodimer-1 (red, 4 μM) for 30 min, followed by rinsing with PBS. For immunocytochemistry, cells were fixed (4% paraformaldehyde (Santa Cruz), 15 min, room temperature), permeabilized (0.2% Triton X-100 (Thermo Fisher), 15 min, room temperature), and blocked (3% bovine serum albumin (Sigma-Aldrich), 1 h). After that, cells were incubated at 4 °C overnight with mouse anti-cardiac troponin T antibody (1:100, Invitrogen MS-295-P1), and rabbit anti-Connexin-43 antibody (Abcam, ab11370). After washing three times with PBS, cells were stained for 1 h at room temperature with Alexa Fluor 568 conjugated goat anti-mouse antibody (1:500, Invitrogen A-11004) and Alexa Fluor 488 anti-rabbit secondary antibodies (1:500, Invitrogen A-11004). Cells were rinsed with PBS and treated with DAPI mounting media (VectaShield) solution for nuclear staining. All the samples were imaged by a scanning laser confocal microscope (Eclipse Ni, Nikon).

### Patterning ANF-PPy electrodes for bioelectrical stimulations

For bioelectrical stimulations on CMs, patterned ANF-PPy bioelectrodes were printed on a PDMS mold. Specifically, patterned SU-8 photoresist (300 μm thickness) on a silicon wafer was fabricated by the standard photolithography approach. These patterns were transferred to a PDMS mold by pouring the liquid PDMS mixture (a weight ratio of 10:1 between silicone elastomer and curing agent, Dow Corning) on the silicon wafer with a height of liquid PDMS of 1.3 mm. After curing at 80 °C for 2 h, the PDMS mold was peeled off from the substrate and punched two holes at specified positions, denoted as the inlet and outlet. The PDMS surface with microgrooves was combined with a water-soluble tape (3 M) to generate microchannels by pressing PDMS gently to allow conformal contact with the tape for 10 min. ANF dispersion was infused slowly into microchannels with a syringe which was connected to the inlet by a PVC tube. Then, the whole setup was soaked in DI water for 24 h to remove the tape and solidify ANF dispersion. PPy was incorporated into the ANF network by treatment of Py (0.6 M) and FeCl<sub>3</sub> (0.72 M) solutions, with the same procedures for the fabrication of ANF-PPy. The excess PPy nanoparticles attached on PDMS surface were removed by placing the device under running tap water.

The pacing device composed of two linear ANF-PPy electrodes on a PDMS substrate was fastened on the bottom of a Petri dish (60 mm diameter) with silicone adhesive. After sterilization with 75% ethanol solution and thorough rinsing with PBS, the device surface was treated with gelatin solution (0.1%, Sigma-Aldrich) under 37 °C for 1 h to promote cell attachment. CMs (2 × 10<sup>5</sup> cells in 25 μL media) were seeded between two parallel electrodes on PDMS and incubated for 1 h before adding CM-specific media. For observing the response of CMs under electrical stimulation, intracellular calcium transient imaging was conducted with Fluo-4 AM (Invitrogen) to label calcium ions in CMs. Three days after cell seeding, the device was washed twice with PBS and subsequently incubated in the calcium indicator media containing fluo-4 AM (10 μM) and Pluronic F-127 (0.1%, Sigma-Aldrich) in Hank's Balanced Salt Solution for 30 min at 37 °C. After that, the device was washed with media, and electrical stimulation of 5-ms-duration monophasic square-wave pulses was delivered at an amplitude of 2.5 V by the stimulator (ME2100, Multi Channel Systems) which was connected to ANF-PPy electrodes by two test leads. The responses of CMs upon electrical stimulation of 2 Hz pacing frequency were recorded continuously in a live-cell imaging chamber with a fluorescence microscope (LS720, Etaluma). Videos were analyzed using ImageJ software.

### Data availability

The data that support the plots in this paper and other findings of this study are available from the corresponding authors upon reasonable request.

## Code availability

All the custom codes deemed central to the conclusions are available from the corresponding authors upon reasonable request.

Received: 17 June 2024; Accepted: 2 September 2024;

Published online: 09 September 2024

## References

- Pu, X. et al. Ultrastretchable, transparent triboelectric nanogenerator as electronic skin for biomechanical energy harvesting and tactile sensing. *Sci. Adv.* **3**, e1700015 (2017).
- Ma, L. et al. Super-stretchable zinc–air batteries based on an alkaline-tolerant dual-network hydrogel electrolyte. *Adv. Energy Mater.* **9**, 1803046 (2019).
- Liu, Y. et al. Soft and elastic hydrogel-based microelectronics for localized low-voltage neuromodulation. *Nat. Biomed. Eng.* **3**, 58–68 (2019).
- Wang, W. et al. Neuromorphic sensorimotor loop embodied by monolithically integrated, low-voltage, soft e-skin. *Science* **380**, 735–742 (2023).
- Walker, B. W. et al. Rational design of microfabricated electroconductive hydrogels for biomedical applications. *Prog. Polym. Sci.* **92**, 135–157 (2019).
- Park, J. et al. Electrically conductive hydrogel nerve guidance conduits for peripheral nerve regeneration. *Adv. Funct. Mater.* **30**, 2003759 (2020).
- Wang, L. et al. Functionalized helical fibre bundles of carbon nanotubes as electrochemical sensors for long-term in vivo monitoring of multiple disease biomarkers. *Nat. Biomed. Eng.* **4**, 159–171 (2020).
- Guo, S. et al. Integrated contact lens sensor system based on multifunctional ultrathin MoS<sub>2</sub> transistors. *Matter* **4**, 969–985 (2021).
- Zhou, T. et al. 3D printable high-performance conducting polymer hydrogel for all-hydrogel bioelectronic interfaces. *Nat. Mater.* **22**, 895–902 (2023).
- Yao, B. et al. Ultrahigh-conductivity polymer hydrogels with arbitrary structures. *Adv. Mater.* **29**, 1700974 (2017).
- Fang, Y. et al. Micelle-enabled self-assembly of porous and monolithic carbon membranes for bioelectronic interfaces. *Nat. Nanotechnol.* **16**, 206–213 (2021).
- Yuk, H., Lu, B. & Zhao, X. Hydrogel bioelectronics. *Chem. Soc. Rev.* **48**, 1642–1667 (2019).
- Hua, M. et al. Tough-hydrogel reinforced low-tortuosity conductive networks for stretchable and high-performance supercapacitors. *Adv. Mater.* **33**, 2100983 (2021).
- He, H. et al. Hybrid assembly of polymeric nanofiber network for robust and electronically conductive hydrogels. *Nat. Commun.* **14**, 759 (2023).
- Cogan, S. F. Neural stimulation and recording electrodes. *Annu. Rev. Biomed. Eng.* **10**, 275–309 (2008).
- Hur, J. et al. Polypyrrole/agarose-based electronically conductive and reversibly restorable hydrogel. *ACS Nano* **8**, 10066–10076 (2014).
- Manjakkal, L., Pullanchiyodan, A., Yogeswaran, N., Hosseini, E. S. & Dahiya, R. A wearable supercapacitor based on conductive PEDOT:PSS-coated cloth and a sweat electrolyte. *Adv. Mater.* **32**, 1907254 (2020).
- Mo, F. et al. A self-healing crease-free supramolecular all-polymer supercapacitor. *Adv. Sci.* **8**, 2100072 (2021).
- Johnson, E. R. et al. Revealing noncovalent interactions. *J. Am. Chem. Soc.* **132**, 6498–6506 (2010).
- Ajmal, C. M., Bae, S. & Baik, S. A superior method for constructing electrical percolation network of nanocomposite fibers: in situ thermally reduced silver nanoparticles. *Small* **15**, 1803255 (2019).
- Chun, K.-Y. et al. Highly conductive, printable and stretchable composite films of carbon nanotubes and silver. *Nat. Nanotechnol.* **5**, 853–857 (2010).
- Han, X. et al. Conductive core–shell aramid nanofibrils: compromising conductivity with mechanical robustness for organic wearable sensing. *ACS Appl. Mater. Interfaces* **11**, 3466–3473 (2019).
- White, S. et al. Electrical percolation behavior in silver nanowire–polystyrene composites: simulation and experiment. *Adv. Funct. Mater.* **20**, 2709–2716 (2010).
- Choi, C. et al. Improvement of system capacitance via weavable superelastic bisrolled yarn supercapacitors. *Nat. Commun.* **7**, 13811 (2016).
- Yao, B. et al. Hydrogel iontronics with ultra-low impedance and high signal fidelity across broad frequency and temperature ranges. *Adv. Funct. Mater.* **32**, 2109506 (2022).
- Pang, A. L., Arsal, A. & Ahmadipour, M. Synthesis and factor affecting on the conductivity of polypyrrole: a short review. *Polym. Adv. Technol.* **32**, 1428–1454 (2021).
- Huang, H. et al. Reinforced conducting hydrogels prepared from the in situ polymerization of aniline in an aqueous solution of sodium alginate. *J. Mater. Chem. A* **2**, 16516–16522 (2014).
- Shi, M. et al. Aqueous organic batteries using the proton as a charge carrier. *Adv. Mater.* **35**, 2302199 (2023).
- McCormick, W. et al. Covalent immobilisation of a nanoporous platinum film onto a gold screen-printed electrode for highly stable and selective non-enzymatic glucose sensing. *Catalysts* **11**, 1161 (2021).
- Cheng, Y., Ren, X., Duan, L. & Gao, G. A transparent and adhesive carboxymethyl cellulose/polypyrrole hydrogel electrode for flexible supercapacitors. *J. Mater. Chem. C* **8**, 8234–8242 (2020).
- Trexler, M. M. et al. Synthesis and mechanical properties of para-aramid nanofibers. *J. Polym. Sci. Part B Polym. Phys.* **57**, 563–573 (2019).
- Xu, L., Zhao, X., Xu, C. & Kotov, N. A. Water-rich biomimetic composites with abiotic self-organizing nanofiber network. *Adv. Mater.* **30**, 1703343 (2018).
- Ni, J. et al. Strong fatigue-resistant nanofibrous hydrogels inspired by lobster underbelly. *Matter* **4**, 1919–1934 (2021).
- He, H. et al. Ultrastrong and multifunctional aerogels with hyperconnective network of composite polymeric nanofibers. *Nat. Commun.* **13**, 4242 (2022).
- He, H. et al. Reversible programming of soft matter with reconfigurable mechanical properties. *Adv. Funct. Mater.* **27**, 1605665 (2017).
- Jiang, Y. et al. Topological supramolecular network enabled high-conductivity, stretchable organic bioelectronics. *Science* **375**, 1411–1417 (2022).
- Park, M. et al. Highly stretchable electric circuits from a composite material of silver nanoparticles and elastomeric fibres. *Nat. Nanotechnol.* **7**, 803–809 (2012).
- Liu, H. et al. Robust and multifunctional kirigami electronics with a tough and permeable aramid nanofiber framework. *Adv. Mater.* **34**, 2207350 (2022).
- He, S. et al. Stretchable supercapacitor based on a cellular structure. *J. Mater. Chem. A* **4**, 10124–10129 (2016).
- Wu, S., Moody, K., Kollipara, A. & Zhu, Y. Highly sensitive, stretchable, and robust strain sensor based on crack propagation and opening. *ACS Appl. Mater. Interfaces* **15**, 1798–1807 (2023).
- Li, Y., Poon, C. C. Y. & Zhang, Y.-T. Analog integrated circuits design for processing physiological signals. *IEEE Rev. Biomed. Eng.* **3**, 93–105 (2010).
- Tandon, N. et al. Electrical stimulation systems for cardiac tissue engineering. *Nat. Protoc.* **4**, 155–173 (2009).
- Chakraborty, P. et al. A self-healing, all-organic, conducting, composite peptide hydrogel as pressure sensor and electrogenic cell soft substrate. *ACS Nano* **13**, 163–175 (2018).

44. Zhang, F. et al. Gelatin-based hydrogels combined with electrical stimulation to modulate neonatal rat cardiomyocyte beating and promote maturation. *Bio Des. Manuf.* **4**, 100–110 (2021).
45. Yoshida, S., Sumomozawa, K., Nagamine, K. & Nishizawa, M. Hydrogel microchambers integrated with organic electrodes for efficient electrical stimulation of human iPSC-derived cardiomyocytes. *Macromol. Biosci.* **19**, 1900060 (2019).
46. Vasseti, D., Pagliai, M. & Procacci, P. Assessment of GAFF2 and OPLS-AA general force fields in combination with the water models TIP3P, SPCE, and OPC3 for the solvation free energy of druglike organic molecules. *J. Chem. Theory Comput.* **15**, 1983–1995 (2022).
47. Nian, B., Xu, Y. J. & Liu, Y. Molecular dynamics simulation for mechanism revelation of the safety and nutrition of lipids and derivatives in food: State of the art. *Food Res. Int.* **145**, 110399 (2021).
48. Han, L. et al. Transparent, adhesive, and conductive hydrogel for soft bioelectronics based on light-transmitting polydopamine-doped polypyrrole nanofibrils. *Chem. Mater.* **30**, 5561–5572 (2018).
49. Lu, T. & Chen, F. Multiwfn: a multifunctional wavefunction analyzer. *J. Comput. Chem.* **33**, 580–592 (2012).
50. Liu, J. et al. Hydrogen-bonding regulated supramolecular chirality with controllable biostability. *Nano Res.* **15**, 2226–2234 (2022).
51. Valdés-Tresanco, M. S., Valdés-Tresanco, M. E., Valiente, P. A. & Moreno, E. gmx\_MMPBSA: a new tool to perform end-state free energy calculations with GROMACS. *J. Chem. Theory Comput.* **17**, 6281–6291 (2021).

## Acknowledgements

The work was supported by grants from Hetao Shenzhen-Hong Kong Science and Technology Innovation Cooperation Zone Shenzhen Park Project (HZQB-KCZY-2021017), the central government-guided special funds for local scientific and technological development (226Z2603G), the Natural Science Foundation of Jiangsu Province (BK20241414), Research Grants Council (RGC) (Project 17200320, 17200722, 17201523, and C6004-22Y) and Environment and Conservation Fund (project 125/2021). This work was also supported by the Health@InnoHK program of the Innovation and Technology Commission of the Hong Kong SAR Government. The authors thank Professor Wending Pan for their assistance in the electrochemical characterization.

## Author contributions

Huimin He and Yaqing Chen: Conceptualization, Data curation, Formal analysis, Investigation, Methodology, Writing – original draft, Writing – review & editing. Aoyang Pu, Li Wang, Wenxiu Li, Xiaoyu Zhou, Chuyang Tang, Kiwon Ban: Data curation, Investigation, Methodology. Mengsu Yang and Lizhi Xu: Conceptualization, Formal analysis, Investigation, Supervision, Validation, Writing – original draft, Writing – review & editing.

## Competing interests

The authors declare no competing interests.

## Additional information

**Supplementary information** The online version contains supplementary material available at <https://doi.org/10.1038/s41528-024-00346-8>.

**Correspondence** and requests for materials should be addressed to Mengsu Yang or Lizhi Xu.

**Reprints and permissions information** is available at <http://www.nature.com/reprints>

**Publisher's note** Springer Nature remains neutral with regard to jurisdictional claims in published maps and institutional affiliations.

**Open Access** This article is licensed under a Creative Commons Attribution 4.0 International License, which permits use, sharing, adaptation, distribution and reproduction in any medium or format, as long as you give appropriate credit to the original author(s) and the source, provide a link to the Creative Commons licence, and indicate if changes were made. The images or other third party material in this article are included in the article's Creative Commons licence, unless indicated otherwise in a credit line to the material. If material is not included in the article's Creative Commons licence and your intended use is not permitted by statutory regulation or exceeds the permitted use, you will need to obtain permission directly from the copyright holder. To view a copy of this licence, visit <http://creativecommons.org/licenses/by/4.0/>.

© The Author(s) 2024